ACS APPLIED MATERIALS & INTERFACES

Research Article

www.acsami.org

^{177}Lu-Labeled Cerasomes Encapsulating Indocyanine Green for Cancer Theranostics

Lijia Jing,[⊥,#] Jiyun Shi,[‡,§,#] Di Fan,[‡] Yaqian Li,[∥] Renfa Liu,[†] Zhifei Dai,[*,†] Fan Wang,[*,‡,§] and Jie Tian[*,∥]

[†]Department of Biomedical Engineering, College of Engineering, Peking University, Beijing 100871, China

[‡]Department of Radiation Medicine, Basic Medical Sciences, Peking University, Beijing 100191, China

[§]Interdisciplinary Laboratory, Institute of Biophysics, Chinese Academy of Sciences, Beijing 100101, China

[∥]Key Laboratory of Molecular Imaging, Institute of Automation, The State Key Laboratory of Management and Control for Complex Systems, Chinese Academy of Sciences, Beijing 100190, China

[⊥]School of Life Science and Technology, Harbin Institute of Technology, Harbin 150080, China

Supporting Information

ABSTRACT: This Article reported the fabrication of a robust theranostic cerasome encapsulating indocyanine green (ICG) by incorporating 1,2-distearoyl-*sn*-glycero-3-phosphoethanolamine-*N*-[carboxy(polyethylene glycol)2000]-1,4,7,10-tetraazacyclododecane-1,4,7,10-tetraacetic acid monoamide (DSPE-PEG$_{2000}$-DOTA), followed by chelating radioisotope of ^{177}Lu. Its applications in optical and nuclear imaging of tumor uptake and biodistribution, as well as photothermal killing of cancer cells, were investigated. It was found that the obtained cerasome could act efficiently as fluorescence contrast agent as well as nuclear imaging tracer. Encapsulating ICG into cerasome could protect ICG from degradation, aggregation, and fast elimination from body, resulting in remarkable improvement in near-infrared fluorescence imaging, photothermal stability, and in vivo pharmacokinetic profile. Both fluorescence and nuclear imaging showed that such agent could selectively accumulate in tumor site after intravenous injection of the cerasome agent into Lewis lung carcinoma tumor bearing mice, resulting in efficient photothermal ablation of tumor through a one-time NIR laser irradiation at the best time window. The ability to track the uptake of cerasomes on a whole body basis could provide researchers with an excellent tool for developing cerasome-based drug delivery agents, especially the strategy of labeling cerasomes with theranostic radionuclide ^{177}Lu, enabling the ability of the ^{177}Lu-labeled cerasomes for radionuclide cancer therapy and even the combined therapy.

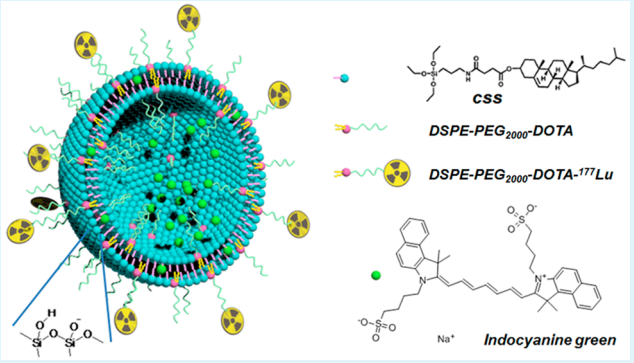

KEYWORDS: *cerasome, indocyanine green, multimodal imaging, photothermal therapy, nanotheranostics*

1. INTRODUCTION

Molecular imaging is a precious tool for molecular biology research and clinical medicine.[1−3] The design, synthesis, and characterization of the proper molecular imaging probes are the priority topic for researchers worldwide in this area.[4,5] Nanoparticles bring the convenience for the design of multifunctional probes due to the flexibility of the sizes and materials. However, most nanoplatforms, such as quantum dots, gold nanoparticles, have been established with inorganic materials, which are difficult to degrade by the human bodies.[6−8]

Liposomes are excellent candidates for molecular imaging because of easy combination with various functionalities and, perhaps most importantly, their biocompatibility.[9] Liposomes appear to be attractive due to the ability to be labeled with radioisotopes, as well as paramagnetic and fluorescent contrast agents. Liposomes have been applied in nuclear imaging by loading radioisotopes or labeling radioisotopes (^{99m}Tc, ^{111}In, ^{67}Ga, ^{18}F, and ^{64}Cu) to study pharmacokinetics or to visualize tumors by SPECT (single-photon emission computed tomography) or PET (positron emission computed tomography) imaging.[9] Most importantly, liposomes have a long-standing history in medical research and clinical practice for use as vehicles to deliver either drugs to target tissue or organ of diseases with high accumulation by producing in nanoscale, long circulating by stealth effect, enhanced permeation and retention (EPR) effect, and specific targeting by modifying with specific ligands or markers.[10,11] However, liposomes still have not attained their full potential as vehicles for therapeutic drugs and contrast agents because of their insufficient morphological stability.

Received: August 23, 2015
Accepted: September 16, 2015
Published: September 23, 2015

DOI: 10.1021/acsami.5b07856
ACS Appl. Mater. Interfaces 2015, 7, 22095−22105

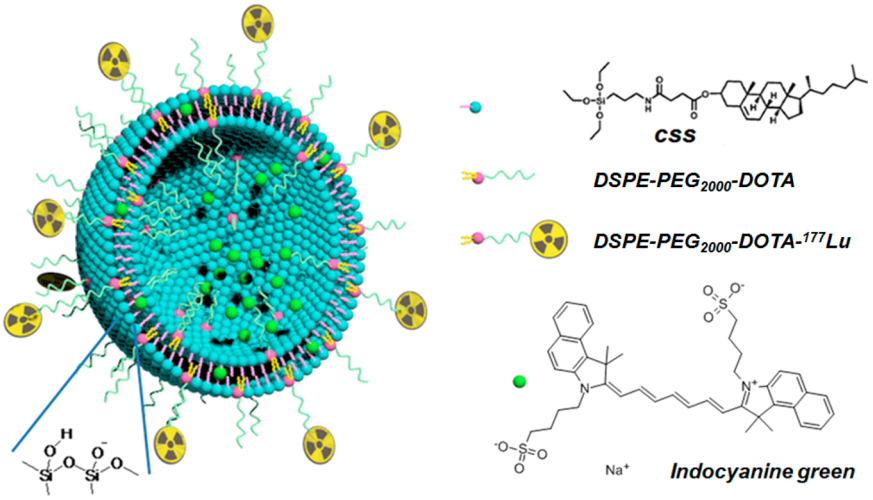

Figure 1. Structural illustration of the ^{177}Lu-labeled cerasomes encapsulating indocyanine green (ICG@DPDCs-^{177}Lu).

Recently, a hybrid liposomal cerasome has attracted broad attention as a novel delivery system because its silica-like surface imparts higher morphological stability than traditional liposomes and its liposomal bilayer reduces the overall rigidity and density greatly as compared to silica nanoparticles.[12−14] Various therapeutic drugs and imaging agents can be easily loaded into the central aqueous core or lipid bilayer of cersomes.[14] Cerasomes combine the advantages of both liposomes and silica nanoparticles but overcome their disadvantages so cerasomes are ideal delivery systems for therapeutic agents. However, the tumor targeting capability and in vivo biobehavior of cerasomes have not been thoroughly studied yet.

Photothermal therapy (PTT) driven by near-infrared (NIR) light has attracted intensive research interest as a promising strategy for cancer treatment due to its noninvasive, targeted, and extracorporeally steerable procedure.[15−19] By applying for photothermal agents, NIR light energy can be converted into hyperpyrexia for target ablation of cancerous tumor without the injury of the surrounding healthy tissue. Especially, recent interests have been focused on the development of multifunctional photothermal agent with appropriate imaging capability for safe and effective PTT treatment.[20−25] In combination with imaging equipment, the imaging capabilities of such agents enable us to visualize the location of cancerous tumor for guiding PTT monitoring of the therapeutic process in real-time, and evaluate the effectiveness after therapy, providing us more opportunities for more specific and individualized cancer treatments.[26−30]

Indocyanine green (ICG) is currently the only Federal Drug Administration (FDA) approved NIR fluorescent agent for clinical applications.[31,32] Because of the strong absorption in the NIR region and the relative high photothermal conversion efficiency, ICG can operate as a photothermal agent for NIR laser-mediated PTT.[33,34] As compared to other reported photothermal agents, ICG takes some advantages due to its clinical approved safety and the intrinsic theranostic capability.[35] However, the aggregate-prone property, poor aqueous stability, fast clearance, and lack of target specificity are still the major challenges for its better application in optical imaging and cancer treatment.[36−39] Attacking such problems head on, numerous nanoparticle (NP) delivery systems have been developed to load ICG to improve its stability and pharmacokinetics, resulting in durable optical imaging and efficient photothermal therapy.[40−43]

In this Article, ^{177}Lu-labeled cerasome encapsulating ICG was engineered from the mixture of cholesteryl succinyl silane and 1,2-distearoyl-*sn*-glycero-3-phospho-ethanolamine-*N*-[carboxy(polyethylene glycol)2000]-1,4,7,10-tetraazacyclododecane-1,4,7,10-tetraacetic acid monoamide (DSPE-PEG$_{2000}$-DOTA) by sol gel reaction and self-assembly process, followed by chelating radioisotope of ^{177}Lu (as shown in Figure. 1). Because of the favorable nuclear characteristics ($T(1/2)$ = 6.71 d, E_g(max) = 0.208 MeV, E_b(max) = 0.497 MeV), ^{177}Lu is an attractive radionuclide for both diagnostic and therapeutic applications. Radiolabeling with ^{177}Lu, cerasome was studied for nuclear imaging and in vivo quantitative evaluation. The encapsulated ICG was used for both NIR fluorescence imaging and photothermal ablation of cancer cells.

2. MATERIALS AND METHODS

2.1. Materials. Indocyanine green (ICG) was obtained from TCI (Shanghai) Development Co., Ltd. 3-(4,5-Dimethylthiazol-2-yl)-2,5-diphenyltetrazolium bromide (MTT), 3,6-di(*O*-acetyl)-4,5-bis[*N*,*N*-bis(carboxymethyl)aminomethyl]fluorescein, tetraacetoxy-methyl ester (Calcein-AM), and 3,8-diamino-5-[3-(diethylmethylammonio)-propyl]-6-pheny-lphenanthridinium diiodide (PI) were purchased from Sigma-Aldrich. 1,2-Distearoyl-*sn*-glycero-3-phosphoethanolamine-*N*-[amino (polyethylene glycol)-2000] (DSPE-PEG$_{2000}$-NH$_2$) was purchased from NOF Corp. (Tokyo, Japan). 1,4,7,10-Tetraazacyclododecane-1,4,7,10-tetraacetic acid mono-*N*-hydroxysuccinimide ester (DOTA-NHS ester) was purchased from Macrocyclics, Inc. (Dallas, TX). All other chemicals and reagents were of analytical grade. Deionized water (18.2 MΩ cm) from a Milli-Q purification system was used in all of the preparations.

2.2. Organic Synthesis. Cholesteryl succinyl silane was synthesized according to our previous method.[44] DSPE-PEG$_{2000}$-DOTA was synthesized according to the following procedure. Briefly, 10 mg of DSPE-PEG$_{2000}$-NH$_2$ and 5 mg of DOTA-NHS ester were dissolved in 2 mL of carbonate buffer solution (pH = 8.5). The resulting solution was magnetically stirred for 36 h at room temperature. When the reaction finished, the solution was sealed in a dialysis bag (molecular cut off: 800 Da) and dialyzed in DI water. Afterward, the target compound was obtained by lyophilizing the solution at −55 °C for 72 h using a freeze-dryer (TFD5505, Ilshin Lab, U.S.). Chemical structures were characterized by LC−MS (Figure S1).

2.3. Fabrication of ICG@DPDCs. Briefly, 5 mg of the mixture of cholesteryl succinyl silane and DSPE-PEG$_{2000}$-DOTA at the molar ratio of 95:5 was dissolved in 100 μL of ethanol, followed by rapid

DOI: 10.1021/acsami.5b07856
ACS Appl. Mater. Interfaces 2015, 7, 22095−22105

injection into 2 mL ICG aqueous solution containing 5, 2.5, 1.25, 0.85, and 0.625 mg of ICG under water-bath sonication to obtain a homogeneous and opalescent suspension, respectively. Afterward, the suspension was further homogenized by probe sonication for 10 min (Sonicator 4000, Misonix) at 40% output amplitude setting in the ice−water bath. ICG@DPDCs was obtained after the removal of excess free ICG using 100 000 Da filters (Millipore).

2.4. Fabrication of ICG@DPDCs-^{177}Lu. In this step, 3 mCi of ^{177}Lu in 50 μL of acetate buffer (pH 4.5) was mixed with 50 μL of ICG@DPDCs (2 mg/mL in pH 4.5 acetate buffer). The mixture was heated at 90 °C for 20 min in a metal bath. Afterward, ICG@DPDCs-^{177}Lu was purified by size exclusion chromatography on a PD Midi-Trap G-25 column using EDTA-dd H_2O solution as eluent. The quality control was carried out with an instant thin layer chromatography (ITLC) method using Gelman Sciences silica gel paper strips and 10 mM EDTA solution as the developing solution.

2.5. Characterization. The typical structure of the nanoparticles was investigated by both transmission electron microscopy (TEM) and scanning electron microscopy (SEM). The size distributions and zeta potentials of the nanoparticles were investigated using a 90Plus/BI-MAS instrument (Brookhaven Instruments Co., U.S.). UV/vis absorption spectra and Fourier transform infrared (FTIR) spectra were measured by a Varian 4000 UV−vis spectrophotometer and a Varian 3000 FTIR spectrophotometer, respectively.

2.6. Photohyperthermic Investigation. Free ICG solution and NPs suspensions of different concentrations in a quartz cuvette (total volume of 3.0 mL) were irradiated by a 808 nm continuous-wave NIR laser (Xi'an Minghui Optoelectronic Technology, China) with output power of 1.5 W. The temperature was recorded by a digital thermometer every 10 s during the irradiation period.

2.7. Cell Culture and Tumor Model. Lewis lung carcinoma cells (LLC cells) were cultured in DMEM Medium (high glucose) with 10% fetal bovine serum (FBS) in the environment of 37 °C and 5% CO_2. C57/BL mice were obtained from Beijing Vital River Laboratories. LCC tumors were created by subcutaneous injection of 2×10^6 LLC cells into the right upper flank of each mouse. All animal experiments were performed in accordance with guidelines of Peking University Animal Care and Use Committee.

2.8. Fluorescence Microscopy. LLC cells were seeded in 12-well plates and incubated with ICG@DPDCs and free ICG at the same ICG concentration of 16 μg/mL (dissolved in fresh medium) for 4 h at the environment of 37 °C and 5% CO_2. Afterward, the cells were washed with PBS (pH 7.4) for observation on a fluorescence microscope (Leica, Germany).

2.9. Fluorescence Intensity. LLC cells were seeded in 12-well plates and incubated with ICG@DPDCs and free ICG at the same ICG concentration of 16 μg/mL (dissolved in fresh medium) for 4 h at the environment of 37 °C and 5% CO_2. Afterward, the cells were digested and counted. The cellular uptake efficiency of ICG@DPDCs and free ICG was evaluated by measuring the fluorescence intensity of a certain amount of cells using a Varian Cary Eclipse fluorescence spectrophotometer, respectively.

2.10. Photohyperthermic Cytotoxicity. To visualize the in vitro photohyperthermic cytotoxicity of ICG@DPDCs and free ICG, LLC cells cultured in a 6-well plate were incubated with ICG@DPDCs and free ICG (2.0 mL per well) for 4 h at the ICG concentrations of 16 μg/mL. After washing with phosphate buffer solution (PBS, 10 mM, pH 7.4) three times, the cells were exposed to NIR laser (1.5 W cm^{-2}, 10 min) and then stained with calcein AM and PI to observe the photohyperthermic cytotoxicity. To further investigate the biocampatibility of ICG@DPDCs and the photohyperthermic cytotoxicity of ICG@DPDCs as compared to free ICG, LLC cells cultured in a 96-well plate were incubated with ICG@DPDCs and free ICG (200 μL per well) for 4 h at different ICG concentrations. After being washed with phosphate buffer solution (PBS, 10 mM, pH 7.4) three times, the cells were exposed to NIR laser (1.5 W cm^{-2}, 10 min) or not. After further 12 h incubation, the viability of the cells was investigated using the standard MTT method. Untreated LLC cells were used as control.

2.11. In Vitro and In Vivo NIR Fluorescence Imaging. NIR fluorescence imaging experiments were performed and analyzed using a IVIS Imaging Spectrum System in combination with IVIS Living Imaging 3.0 software (PerkinElmer, U.S.) at certain parameters (λ_{ex} = 745 nm, λ_{em} = 820 nm, binning = 1, exposure time = 0.1 s). For in vitro imaging, different samples were poured into 1.5 mL tubes and imaged. For in vivo imaging, LLC tumor bearing mice (18−20 g) were anesthetized by isoflurane. Next, 0.2 mL of ICG@DPDCs dispersion (2 mg/mL of the NPs; 0.2 mg/mL of ICG) was intravenously injected. The NIR fluorescence images of tumor region were acquired at different time points after injection. All animal procedures were in agreement with institutional animal use and care committee and carried out ethically and humanely.

2.12. In Vivo NanoScan SPECT/CT Imaging. LLC tumor-bearing mice (18−20 g) were used for the in vivo whole-body nuclear imaging experiment. After tail vein injection of 0.2 mL of ICG@DPDCs-^{177}Lu dispersion (^{177}Lu 11.1 MBq, 2 mg/mL of the NPs), images were captured at 1, 4, 8, 12, 24, 36, and 48 h postinjection (p.i.). For imaging, the mice were anesthetized (1.5% isoflurane and 0.5−1 L per minute oxygen) and imaged using a nanoScan SPECT/CT in vivo preclinical imager (Mediso, Budapest, Hungary) fitted with 2 mm pinhole collimators in helical scanning mode (20 projections, 30 min). The CT projections were recorded at 55 kV and 170 μA of tube voltage and current, respectively, in the cone-beam CT subsystem of the instrument, with an isotropic voxel size set at 72 μm. All images were reconstructed and fused using Nucline software (Mediso Imaging System, Budapest, Hungary).

2.13. Pharmacokinetics and Biodistribution. For the pharmacokinetics studies, seven normal BALB/c mice were used as one group for the experiment of the blood clearance of ICG@DPDCs-^{177}Lu. A total of 0.2 mL of ICG@DPDCs-^{177}Lu dispersion (^{177}Lu 0.37 MBq, 2 mg/mL of the NPs) was administered intravenously to each mouse. Animals were anesthetized with intraperitoneal injection of sodium pentobarbital at a dose of 45.0 mg/kg. Blood was harvested from orbital sinus at 1, 10, 20, 30, 60, 90, 120, 180, 240, 360, 1440, 2880, and 4320 min, weighed, and measured for radioactivity in a γ-counter (Wallac 1470−002, PerkinElmer, Finland). The radioactivity in blood was calculated as a percentage of the injected dose per gram (% ID/g). Biodistribution experiment was also performed to quantificationally study the in vivo distribution of ICG@DPDCs-^{177}Lu in all of the organs and the uptake in tumor area. A total of 16 LLC tumor-bearing mice were randomly divided into four groups, each of them containing four individuals. A total of 0.2 mL of ICG@DPDCs-^{177}Lu dispersion (^{177}Lu 0.37 MBq, 2 mg/mL of the NPs) was administered intravenously to each mouse. Animals were anesthetized with intraperitoneal injection of sodium pentobarbital at a dose of 45.0 mg/kg. Time-dependent biodistribution studies were carried out by sacrificing mice at 4, 24, 48, and 72 h p.i. Blood, heart, liver, spleen, kidney, stomach, intestine, muscle, bone, and tumor were harvested, weighed, and measured for radioactivity in a γ-counter. The organ uptake was calculated as a percentage of injected doses per gram of wet tissue mass (% ID/g).

2.14. In Vivo Photothermal Therapy. Mice bearing LLC tumors were randomly divided into four groups (n = 6) including ICG@DPDCs + laser group, free ICG + laser group, PBS + laser group, and agent only group. After intravenous injection of 100 μL of an aqueous solution of ICG@DPDCs or free ICG (at the same dose of 2 mg/kg of ICG), tumors in the two treatment groups were irradiated by 808 nm continuous-wave diode NIR laser at 1.5 W cm^{-2} for 10 min. During the irradiation period, a thermometer probe was inserted into the tumor for dynamically recording the temperature of the tumor. After photothermal treatment, the tumor diameters were measured by a caliper every 3 days. Tumor volumes were calculated according to the formulation: ((tumor length) × (tumor width)^2)/2.

2.15. Toxicology Evaluations. Healthy C57/BL mice were injected with ICG@DPDCs at a dose of 20 mg/kg, which was equal to the treatment and imaging dose. Several mice were sacrificed to investigate blood biochemistry assay after injection of ICG@DPDCs for 10 days. Major organs including liver, heart, kidney, spleen, and lung were collected at different time points for investigating the histopathology changes after H&E staining.

DOI: 10.1021/acsami.5b07856
ACS Appl. Mater. Interfaces 2015, 7, 22095−22105

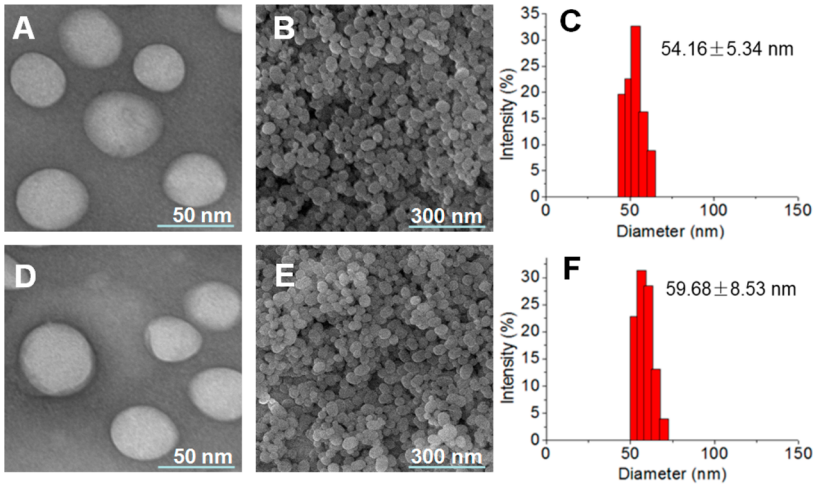

Figure 2. TEM image (A), SEM image (B), and size distribution (C) of the ICG@DPDCs; TEM image (D), SEM image (E), and size distribution (F) of ICG@DPDCs-^{177}Lu.

2.16. Statistical Analysis. Statistical analyses were performed using Micorcal Origin 8.0 (Microcal Software). The results were compared using one-way analysis of variance (ANOVA) (*$p < 0.05$ and **$p < 0.01$).

3. RESULTS AND DISCUSSION

3.1. Preparation and Characterization of the Nanoparticles. ICG@DPDCs were prepared by sol−gel reaction and self-assembly process from cholesteryl succinyl silane and DSPE-PEG$_{2000}$-DOTA at the molar ratio of 95%:5%. After hydrolyzing the triethoxysilyl group, the lipid bilayer self-assembled via the strong hydrophobic interaction and rigidified via in situ sol−gel reaction ($Si{-}OCH_2CH_3 + H_2O \rightarrow Si{-}OH + CH_3CH_2OH$ followed by $2Si{-}OH \rightarrow Si{-}O{-}Si + H_2O$) on the vesicle surface upon ultrasonication. Both TEM and SEM images revealed that ICG@DPDCs were well-defined and spherical before and after chelating ^{177}Lu (Figure 2A,B,D,E). In agreement with TEM and SEM measurements, the dynamic light scattering data showed that ICG@DPDCs possessed a narrow size distribution of 54.16 ± 5.34 nm, favorable to the enhanced permeability and retention (EPR) effect in tumor vasculature for passive targeting (Figure 2C). As shown in Figure S2, the two distinctive absorption bands at 1100 and 950 cm^{-1}, attributed to the vibration of Si−OH group and Si−O−Si, proved the presence of a highly polymerized silicate network around the surface of ICG@DPDCs. Resembling silica particles, ICG@DPDCs fabricated at different mass ratios of ICG to lipid were negatively charged, and the zeta-potentials were in the range from −28.85 ± 3.64 to −32.12 ± 4.31 mV due to deprotonation of the silanol groups on the ICG@DPDCs surface (Table 1).

Table 1. Zeta Potential, Loading Capacity (LC), and Encapsulation Efficiency (EE) of ICG@DPDCs at Different Mass Ratios of ICG to Lipid

mass ratios of ICG to lipid	LC (%)	EE (%)	zeta potentials (mV)
1:1	23.48 ± 6.77	24.66 ± 9.37	−31.46 ± 3.89
1:2	18.51 ± 8.42	36.09 ± 6.98	−29.86 ± 3.15
1:4	12.66 ± 6.32	51.34 ± 7.55	−32.12 ± 4.31
1:6	10.23 ± 0.88	60.43 ± 9.31	−28.85 ± 3.64
1:8	8.23 ± 9.41	62.22 ± 8.93	−29.42 ± 4.23

3.2. UV−Vis Absorption and Fluorescence Properties. ICG molecules could be easily loaded into the lipid bilayer and empty core domain of DPDCs nanoparticles due to their amphiphilic structure and good water solubility. It was found that the mass ratios of ICG to lipids have effects on the loading capacity and the encapsulation efficiency. With increasing the mass ratio of ICG to lipids, the loading capacity increased and the encapsulation efficiency decreased (Table 1). Figure 3A shows the UV−vis absorption spectra of ICG@DPDCs encapsulating different amounts of ICG. The broad absorption band between 650 and 900 nm suggests that ICG@DPDCs would be suitable for photothermal therapy with the light in the NIR region, where there is minimum light absorption in tissues. As shown in Figure 3B, the encapsulation of ICG into the mixed cerasomes of DPDCs led to a red shift of the characteristic maximum absorption peak of ICG (from 779 to 789 nm). The red shift might be attributed to the strong interaction between ICG molecules and cerasomes. The aggregation of ICG molecules usually accompanies the occurrence of fluorescence quenching. As shown in Figure 3C and D, the fluorescence intensity was remarkably enhanced after loading into the DPDCs as compared to free ICG. In addition, the fluorescence intensity of ICG@DPDCs increased with decreasing the mass ratio of ICG to lipids. It can be explained that the amphiphilic molecules in the lipid layer could effectively separate ICG molecule from each other, resulting in the red-shifted absorption and the minimized fluorescence quenching.[45] In consideration of the absorbance value, fluorescence intensity, as well as the loading capacity and the encapsulation efficiency, ICG@DPDCs fabricated at the mass ratio (ICG:lipids) of 1:6 were thus chosen for further investigation.

3.3. Structural Stability of the Nanoprticles. Radioisotope of ^{177}Lu can be readily coupled onto the ICG@DPDCs surface. Figure S3 revealed that the radiolabeling yield was 63.66% and the radiochemical purity after purification was 99.93%. Figure S4 showed the strong chelating between ^{177}Lu and ICG@DPDCs; less than 4% of ^{177}Lu was released from the NPs after incubation in PBS for 48 h. Because of the presence of rigid polyorganosiloxane networks, ICG@DPDCs-^{177}Lu can keep structural integrity (Figure 2D and E), but the diameter of ICG@DPDCs-^{177}Lu had an increase of about 5 nm after chelating ^{177}Lu in a rather harsh environment (pH 4.5, 90 °C)

DOI: 10.1021/acsami.5b07856
ACS Appl. Mater. Interfaces 2015, 7, 22095−22105

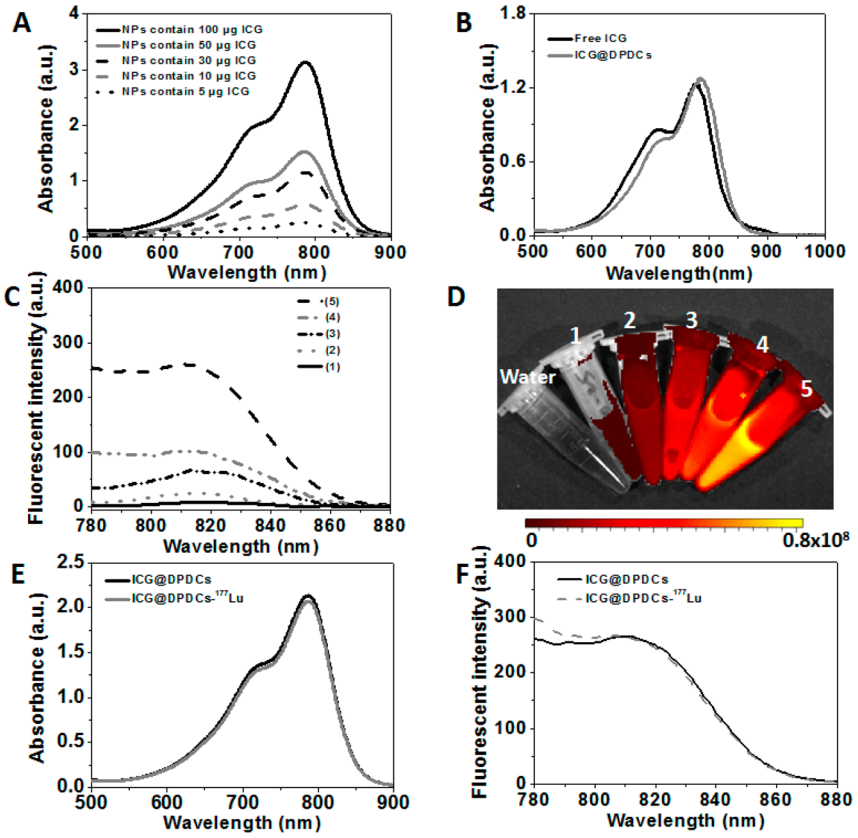

Figure 3. (A) UV−vis absorption spectra of ICG@DPDCs encapsulating different amounts of ICG. (B) UV−vis absorption spectra of free ICG and ICG@DPDCs. (C) Fluorescence spectra of free ICG (1) and ICG@DPDCs prepared at different mass ratios of ICG to lipid: (2) 1:1, (3) 1:2, (4) 1:4, (5) 1:6; free ICG and all ICG@DPDCs samples have the same ICG concentration of 0.2 mg/mL. (D) NIR fluorescence images of water, free ICG (1), and ICG@DPDCs prepared at different mass ratios of ICG to lipid: (2) 1:1, (3) 1:2, (4) 1:4, (5) 1:6; free ICG and all ICG@DPDCs samples have the same ICG concentration of 0.2 mg/mL. (E) UV−vis absorption spectra of ICG@DPDCs before and after chelating radioisotope of ^{177}Lu. (F) Fluorescence spectra of ICG@DPDCs before and after chelating radioisotope of ^{177}Lu.

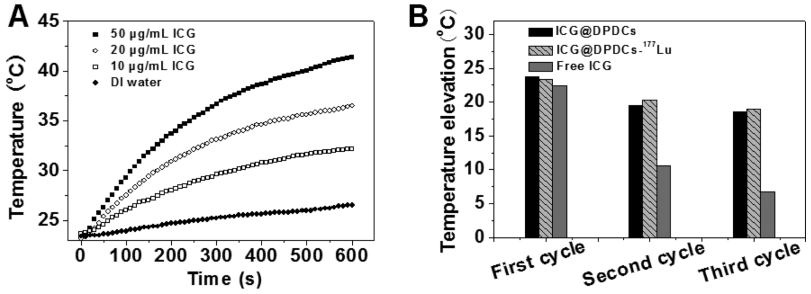

Figure 4. (A) Temperature elevation of DI water and ICG@DPDCs-^{177}Lu with ICG concentrations of 10, 20, and 50 μg/mL over a period of 10 min of exposure to NIR laser (808 nm, 1.5 W). (B) Temperature elevation of ICG@DPDCs, ICG@DPDCs-^{177}Lu and free ICG at the same ICG concentration of 55 μg/mL with three laser on/off cycles of NIR laser irradiation.

as shown in Figure 2F. Almost no decrease of absorbance and fluorescence intensity was seen during the process of radiolabeling, indicating that the cerasomal vesicles could protect ICG from leaking and degradation in high temperature (Figure 3E and F). The structural stability of NPs was evaluated by the widely used surfactant dissolution method.[14] When 10 equiv of the Triton X-100 was added to 1,2-distearoyl-*sn*-glycero-3-phosphoethanolamine (DSPE)-based liposomes, a significant reduction in the hydrodynamic diameter was seen, indicating the rapid collapse of the liposomes. In contrast, both ICG@DPDCs and ICG@DPDCs-^{177}Lu showed almost no change in their hydrodynamic diameters for a long time even in the presence of 50 equiv of Triton X-100 (Figure S5). It suggested the excellent architectural stability of the cerasomes.

3.4. Photohyperthermic Behavior of ICG@DPDCs-^{177}Lu. The photohyperthermic behavior of ICG@DPDCs-^{177}Lu was investigated under the irradiation of 808 nm continuous-wave NIR laser at the output power of 1.5 W. Figure 4A showed the temperature collected by a digital thermometer every 10 s under irradiation of DI water and ICG@DPDCs-^{177}Lu with ICG concentrations of 10, 20, and 50 μg/mL. It was found that the temperature elevated with increasing the irradiation time and concentration of ICG@DPDCs-^{177}Lu. The temperature elevations of 8.9, 17.1, and 20.2 °C were achieved after 10 min NIR laser irradiation of

DOI: 10.1021/acsami.5b07856
ACS Appl. Mater. Interfaces 2015, 7, 22095−22105

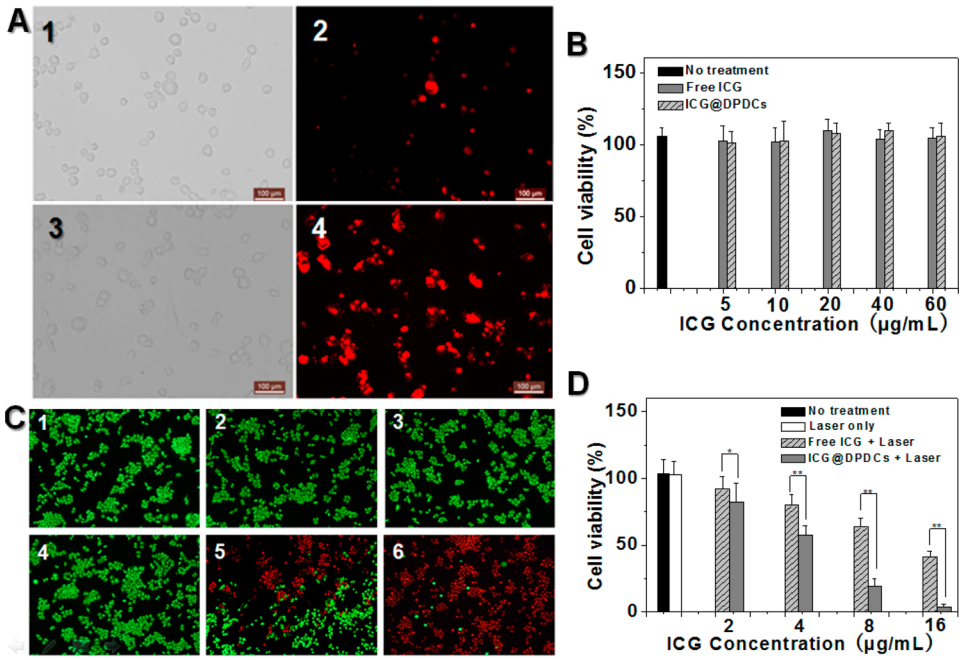

Figure 5. (A) Fluorescence microscopy images of LLC cells after incubation with free ICG and ICG@DPDCs at the ICG concentration of 16 μg/mL for 4 h: bright field image (1) and fluorescence image (2) of free ICG treated LLC cells, and bright field image (3) and fluorescence image (4) of ICG@DPDCs treated LLC cells. (B) Viability of LLC cells after the treatment with free ICG and ICG@DPDCs at different ICG concentrations for 48 h. (C) Fluorescence microscopy images of the photohyperthermic cytotoxicity of free ICG and ICG@DPDCs on LLC cells with different treatments: (1) no treatment, (2) laser only, (3) free ICG only, (4) ICG@DPDCs only, (5) free ICG + laser, and (6) ICG@DPDCs + laser. (D) Viability of LLC cells after the treatment with free ICG and ICG@DPDCs at different ICG concentrations under NIR laser irradiation (10 min, 808 nm, 1.5 W cm^{-2}). Data shown as means ± SD (n = 3,**p < 0.01, and *p < 0.05).

ICG@DPDCs-^{177}Lu at the ICG concentrations of 10, 20, and 50 μg/mL, respectively. In contrast, no obvious temperature elevation was observed when DI water was exposed to the same laser irradiation. This result demonstrated the excellent photothermal efficiency of ICG@DPDCs-^{177}Lu.

For comparative investigation of the photostability of ICG@DPDCs, ICG@DPDCs-^{177}Lu, and free ICG molecules under the exposure of NIR light, treatments containing three cycles of NIR laser on/off were used. Solutions of ICG@DPDCs, ICG@DPDCs-^{177}Lu, and free ICG were exposed to NIR laser for 10 min, followed by naturally cooling to room temperature with no NIR laser exposure for 50 min (laser off). Such a laser on/off cycle was repeated three times. At the same ICG concentration of 55 μg/mL, the temperature elevations of 23.7, 19.5, and 18.6 °C for ICG@DPDCs-^{177}Lu solution, 23.4, 20.3, and 19.0 °C for ICG@DPDCs solution, and 22.4, 10.6, and 6.8 °C for free ICG solution were observed after three consecutive cycles of NIR laser on/off, respectively (Figure 4B). For free ICG solution, the temperature elevation rapidly decreased with increasing the number of laser on/off cycles. On the contrary, the temperature elevations were well repeated for both ICG@DPDCs and ICG@DPDCs-^{177}Lu, demonstrating that the encapsulation of ICG inside cerasomal nanoparticles conduced to excellent photostability.

3.5. Photohyperthermic Cytotoxicity of ICG@DPDCs. The cellular uptake of ICG@DPDCs was investigated in comparison with free ICG using fluorescence microscopy before the investigation of their therapeutic potential. Upon excitation by the light of 740 nm, both free ICG and ICG encapsulated in ICG@DPDCs exhibit a red fluorescence. As shown in Figure 5A, after incubation for 4 h, LLC cells incubated with ICG@DPDCs were significantly brighter than free ICG incubated cells, and the fluorescence intensity of the former was evaluated to be 4-fold as much as the latter (Figure S6). This result indicated that ICG@DPDCs can be internalized more efficiently by LLC cells through endocytosis. In comparison with free ICG, the excellent cellular uptake efficiency of ICG@DPDCs is favorable to photothermally ablate cancer cells at the same ICG dosage.

To visualize the photohyperthermic cytotoxicity of ICG@DPDCs in vitro, Lewis lung cancer cell lines (LLC cells) were incubated with the ICG@DPDCs and free ICG for 4 h, followed by exposure to NIR laser (808 nm and 1.5 W cm^2) for 10 min. Various combination treatments with agent and NIR laser were used for comparative study. The photohyperthermic cytotoxicity was evaluated by using the double staining method with calcein AM and PI. Calcein AM can be hydrolyzed into strongly green fluorescent calcein by intracellular esterases in viable cells, while PI can interact with the nucleic acid in dead cells to create strong red fluorescence. After the double staining, red fluorescence representing the death of cancer cells was observed in the combination of both the agent (ICG@DPDCs and free ICG) and the NIR laser, while other combination treatments displayed bright green fluorescence in the entire area (Figure 5C). It suggested that exposing cancer cells to either agent or high intensity NIR laser alone did not compromise cell viability. Upon laser irradiation, the LLC cells incubated with free ICG showed a partial red fluorescence, while the LLC cells incubated with ICG@DPDCs exhibited an entire red fluorescence, indicating a remarkably higher photothermal cytotoxicity of ICG@DPDCs.

To further quantify the photohyperthermic cytotoxicity of ICG@DPDCs, a standard MTT assay was used to evaluate the inhibitory profile of ICG@DPDCs and free ICG against LLC

DOI: 10.1021/acsami.5b07856
ACS Appl. Mater. Interfaces 2015, 7, 22095−22105

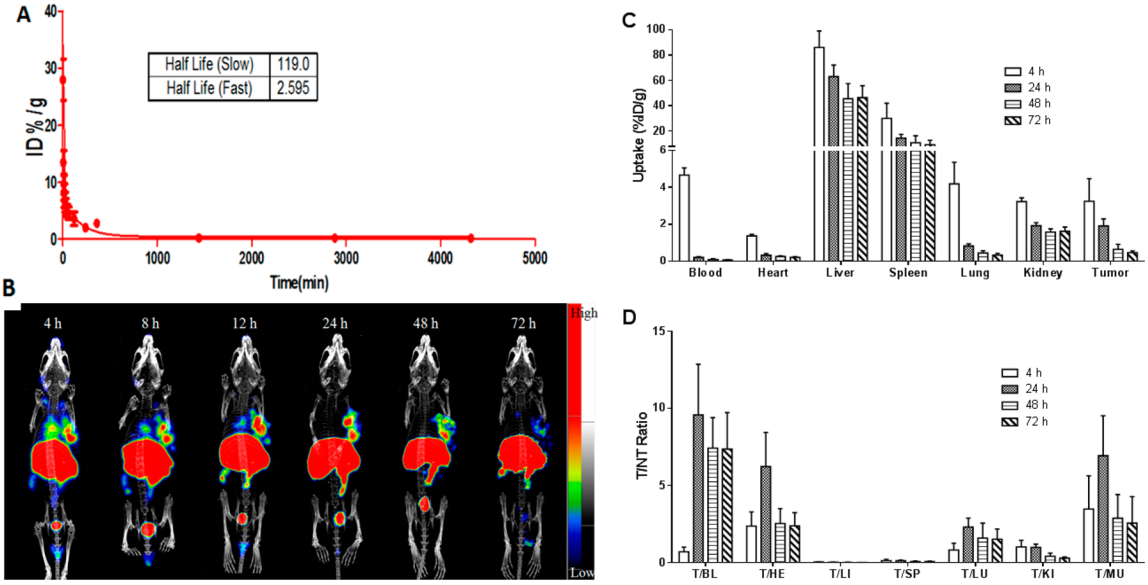

Figure 6. (A) The blood clearance curve of ICG@DPDCs-^{177}Lu. (B) NanoScan SPECT/CT images of LLC tumor bearing mouse at different time points after intravenous injection of ICG@DPDCs-^{177}Lu. Biodistribution (C) and tumor-to-nontargeted tissue ratio (D) of ICG@DPDCs-^{177}Lu in LLC bearing mice at 4, 24, 48, and 72 h p.i.

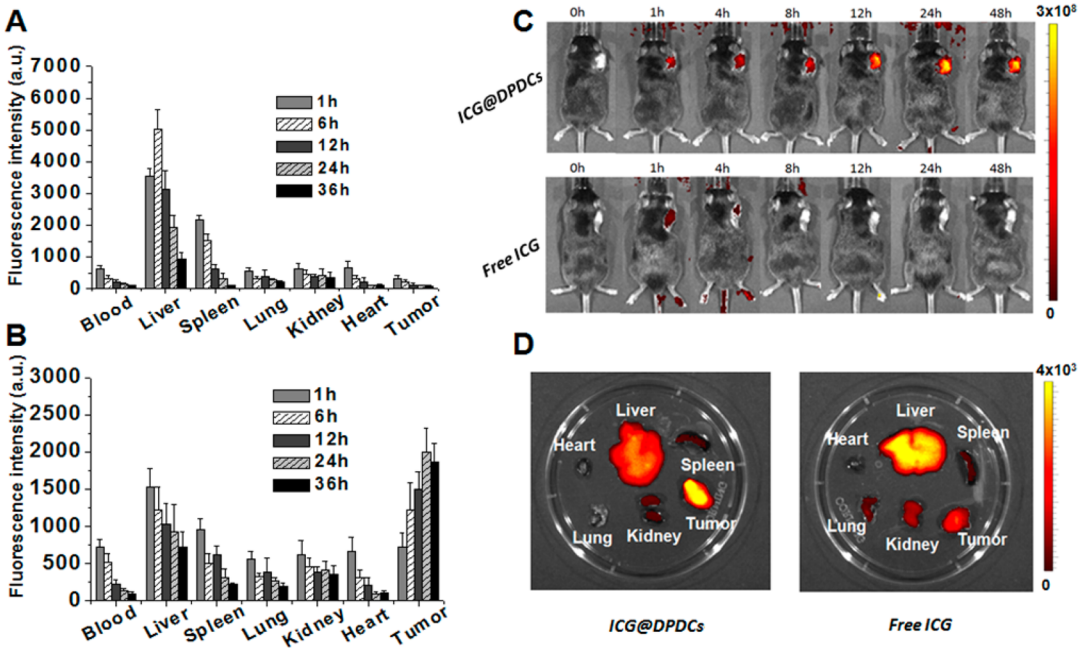

Figure 7. Fluorescence intensity of the major organs at different time points after the injection of free ICG (A) and ICG@DPDCs (B). (C) Fluorescence images of mice bearing LLC tumor at different time points after intravenous injection of ICG@DPDCs and free ICG, respectively. (D) Fluorescence images of tumor and main organs in LLC tumor bearing mice after 24 h injection of free ICG and ICG@DPDCs, respectively.

cells under NIR laser irradiation. Without NIR laser irradiation, ICG@DPDCs and free ICG showed almost no toxicity to LLC cells, demonstrating the high biocompatibility of the agent alone (Figure 5B). However, under a simultaneous treatment with agent and NIR laser (1.5 W cm^{-2}, 10 min), the viability of LLC cells significantly decreased as the concentrations of ICG@DPDCs and free ICG increased. It was found that the photothermal cytotoxicity of ICG@DPDCs was obviously higher than that of free ICG at all ICG concentrations. At the highest dosage, the cellular viability decreased to about 41.1% for free ICG + laser and about 4.3% for ICG@DPDCs + laser. Thus, our data provided strong evidence that ICG@DPDCs displayed remarkably higher photothermal cytotoxicity in comparison with free ICG through the more efficient cellular endocytosis.

3.6. In Vivo NanoScan SPECT/CT Imaging of ICG@DPDCs-^{177}Lu. To evaluate the feasibility of applying nuclear imaging for dynamically monitoring the accumulation of ICG@DPDCs-^{177}Lu in the tumor region and guiding the photothermal ablation of tumor, a whole-body NanoScan SPECT/CT imaging procedure was performed on LLC tumor-bearing mouse by intravenous injection of ICG@DPDCs-^{177}Lu at the dose of 20 mg/kg (^{177}Lu 11.1 MBq), which was equal to the dose used for NIR fluorescent imaging. Figure 6B showed that

DOI: 10.1021/acsami.5b07856
ACS Appl. Mater. Interfaces 2015, 7, 22095−22105

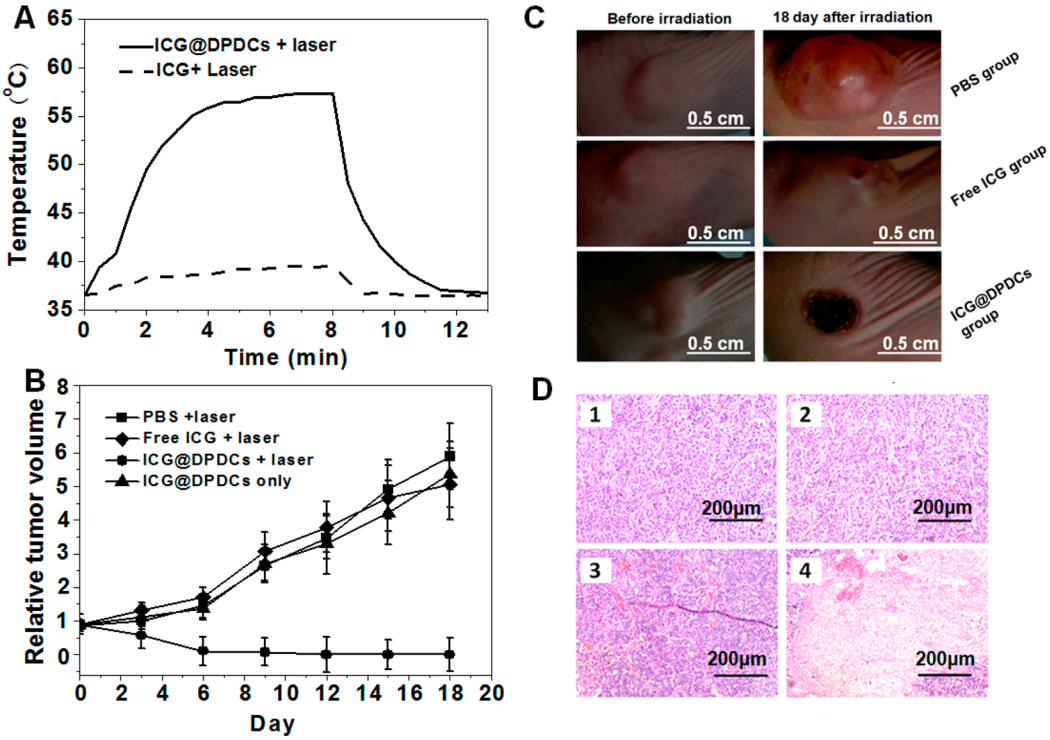

Figure 8. (A) Temperature elevation curves of the mice tumor measured by thermographic probe after treatments with free ICG or ICG@DPDCs upon exposure to the 808 nm laser at a power density of 1.5 W/cm^2. (B) The tumor growth curves of different groups (■, PBS + laser; ◆, free ICG + laser; ●, ICG@DPDCs + laser; ▲, ICG@DPDCs only). (C) The representative tumor photographs of each group were recorded before and after treatment. (D) Representative histological section of tumors in mice with different treatments: (1) PBS + laser, (2) ICG@DPDCs only, (3) free ICG + laser, and (4) ICG@DPDCs + laser.

tumor was clearly visulized at all test time points. Besides tumor, the main accumulation of ICG@DPDCs-^{177}Lu was found in the liver and spleen, which is in agreement with the in vivo uptake characteristics of nanomaterials. Because of clearance of the radiotracer from the background, the contrast of tumor region to adjacent tissue increased gradually throughout the 24 h post injection, and reached the maximum at 24 h p.i., then gradually decreased to 72 p.i., which is consistent with the result of NIR fluorescent imaging. With the help of the 3D-reconstructed SPECT/CT images, the position of tumor and the accumulation of ICG@DPDCs-^{177}Lu in tumor region contrasted with clear background could be easily visualized, which can help the researcher find the best time-window for guiding the photothermal therapy through the NanoScan SPECT/CT imaging.

3.7. Pharmacokinetics and Biodistribution. To quantificationally study the in vivo biobehavior of ICG@DPDCs-^{177}Lu, a dose of 0.2 mL of ICG@DPDCs-^{177}Lu dispersion (2 mg/mL of the NPs containing 0.37 MBq of ^{177}Lu) was administrated to the normal BALB/c mice and LLC tumor-bearing mice, respectively, and the pharmacokinetics and biodistribution experiments were performed at test time points. The blood radioactivity measurements showed that the pharmacokinetics of ICG@DPDCs-^{177}Lu fitted a two-compartment open model with the fast and slow phase half-lives at 2.6 and 119 h during blood circulation, respectively (Figure 6A). The selected quantitative biodistribution and tumor-to-non-tumor ratio data were shown in Figure 6C and D. The detailed biodistribution and target-to-background ratio data are summarized in Tables S1 and S2. The tumor uptake of ICG@DPDCs-^{177}Lu was 3.25 ± 1.22%, 1.91 ± 0.39%, 0.65 ± 0.27%, and 0.47 ± 0.10% ID/g at 4, 24, 48, and 72 h postinjection, respectively. Besides the tumor, the major uptake was found in the liver and spleen, with values of 86.02 ± 13.13%, 63.02 ± 9.11%, 45.57 ± 11.97%, and 46.37 ± 9.44% ID/g for liver, and 29.99 ± 1.98%, 14.44 ± 2.97%, 10.75 ± 5.56%, and 9.17 ± 3.56% ID/g for spleen at 4, 24, 48, and 72 p.i., respectively. The nonspecific uptake in the other tissues (heart, stomach, pancreas, intestine, kidneys) was <5% ID/g at all test time points. Most of the tumor-to-nontargeted tissue ratios showed similar changing tendency, such as the tumor-to-muscle ratio increased from 3.48 ± 2.15 (4 h p.i.) to 6.93 ± 2.60 (24 h p.i.), and then decreased to 2.88 ± 1.53 and 2.57 ± 1.71 at 48 and 72 h p.i., respectively, which was consistent with the SPECT imaging results (Figure 6C,D).

3.8. In Vivo Fluorescence Imaging of ICG@DPDCs. Figure 7A and B showed the fluorescence intensities of vital organs and tumors in mice after the injection of free ICG and ICG@DPDCs, respectively. Obviously, a great difference in the fluorescent distribution was seen between the two mice groups injected with free ICG and ICG@DPDCs. For the free ICG group, the fluorescence signals of liver were much higher than that of tumor and other organs, indicating that free ICG molecules could accumulate mainly in liver and not in tumor because they were absorbed by serum proteins such as albumin and lipoproteins and were selectively trapped at liver.[44] In addition, it was found that the total of fluorescence intensity was remarkably decreased as the time increased, suggesting that free ICG molecules can be fast excreted from liver and other organs, in agreement with the published results.[45] On the contrary, ICG@DPDCs was very different from free ICG molecules. It was observed to increase with time during the 24

DOI: 10.1021/acsami.5b07856
ACS Appl. Mater. Interfaces 2015, 7, 22095−22105

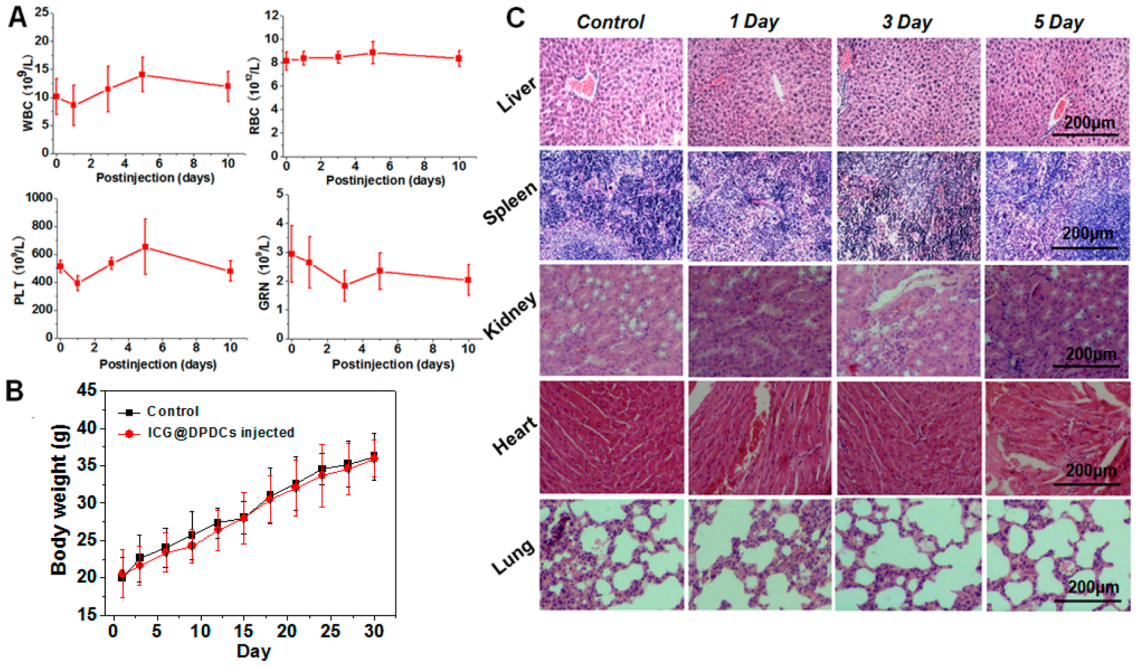

Figure 9. (A) Serum biochemistry assays including white blood cells (WBC), red blood cells (RBC), platelets (PLT), and neutrophile granulocyte (GRN) after the injection of ICG@DPDCs. (B) Body weight growth curve of mice after the injection of ICG@DPDCs or not. (C) Histological examinations of liver, spleen, kidney, heart, and lung in mice at different time points after the injection of ICG@DPDCs.

h post injection, providing strong evidence that ICG@DPDCs with suitable size could selectively accumulate in the tumor. It was attributed to the EPR effect in tumor vasculature and the introduction of the PEG molecules onto the surface of ICG@DPDCs, which could inhibit our agent from the macrophage recognition at reticuloendo-thelial system (RES), leading to a prolonged blood circulation time.

A whole body NIR imaging approach was further employed to investigate the tumor targeting capability of ICG@DPDCs on LLC tumor-bearing mice by intravenous injection of ICG@DPDCs at the dose of 20 mg/kg (ICG dose of 2 mg/kg). Figure 7C displayed the fluorescence signal as a function of time for ICG@DPDCs and free ICG delivered systemically via intravenous injections. At 1 and 4 h after injection ICG@DPDCs, only weak fluorescence signals were observed throughout the mouse body. As time increased the fluorescence signals increased and almost located around the tumor after 24 h postinjection, suggesting that a large amount of ICG@DPDCs circulated in the blood circulation and then accumulated at the tumor site. As seen in Figure 7D, a great difference in the tumor distribution was seen between ICG@DPDCs and free ICG molecules after 24 h postinjection through tail vein. ICG@DPDCs showed strong fluorescence signals but only weak signals from the free ICG group in the tumor site. These preliminary data provided a good evidence of the high efficiency of passive tumor targeting of ICG@DPDCs.

However, it is worth noting that the fluorescence intensities of vital organs after the injection of ICG@DPDCs were obviously different from the previous result of SPECT/CT imaging. As reported in the literature, Shi and co-workers confirmed that mesoporous silica nanoparticles (MSNs) could be partly degraded in vivo and excreted through the renal excretion route.[46] Thus, cerasome with single-layer silica-like surface is likely to be degraded in vivo through the same route as MSNs, resulting in a certain degree of ICG leakage after a certain period postinjection. Because of the fast metabolism and excretion rate of ICG, liver and spleen showed decreased fluorescence signals. On the contrary, the tumor site displayed increased fluorescence intensity, which is attributed to the sufficient penetration of the released ICG throughout the tumor, decreasing the fluorescence quenching effect caused by the aggregation of ICG molecules. Such sufficient diffusion of ICG in tumor site is advantaged for photothermal tumor ablation by achieving a homogeneous hyperpyrexia under NIR laser irradiation.

3.9. In Vivo Photothermal Therapy Using ICG@DPDCs.

To evaluate in vivo photothermal therapy using ICG@DPDCs, LLC tumor-bearing mice were divided into four groups, and received the treatments of PBS buffer + NIR laser, free ICG + NIR laser, ICG@DPDCs only, and ICG@DPDCs + NIR laser, respectively. As we know from the above in vivo fluorescence and NanoScan SPECT/CT imaging results, the optimum accumulation of ICG@DPDCs and free ICG in the tumor site could be achieved after the injection of ICG@DPDCs and free ICG for 24 and 1 h, respectively. Hence, mice tumors in ICG@DPDCs + NIR laser and free ICG + NIR laser groups were exposed to the 808 nm laser at a power density of 1.5 W/cm^2 for 10 min at the best therapy window after the injection of ICG@DPDCs and free ICG for 24 and 1 h, respectively. Because of the photothermal effect of ICG@DPDCs, the average temperature of cancerous tumor was rapidly elevated from 36.5 to 57.3 °C under the laser irradiation (Figure 8A), which was high enough to ablate efficiently the cancer cells. In contrast, the temperature in the tumor area treated with free ICG + NIR laser was not obviously affected after laser irradiation (Figure 8A). The therapeutic effectiveness was evaluated by measuring the tumor sizes, and the representative mice photographs of each group were recorded at certain days after treatment (Figure 8B and C). Mice tumors treated with agent only, PBS + laser, and free ICG + laser increased rapidly over 18 days (Figure 8B), indicating that the tumor growth could not be affected by either ICG@DPDCs or NIR laser

DOI: 10.1021/acsami.5b07856
ACS Appl. Mater. Interfaces 2015, 7, 22095−22105

irradiation alone as well as the presence of a low amount of free ICG combined NIR laser irradiation. The absence of a significantly harmful effect by treatment with free ICG combined NIR laser irradiation was not surprising in light of the low mean peak temperatures elevation measured in the tumors during the exposures (Figure 8A). In stark contrast, after treatment with ICG@DPDCs in combination NIR irradiation, the growth of cancerous tumors was significantly inhibited and ceased, leaving black scars at their original sites without showing reoccurrence (Figure 8C). Further hematoxylin and eosin (H&E) staining of tumor slices was carried out for tumors collected immediately after laser irradiation (Figure 8D). As expected, significant cancer cell damage, such as karyorrhexis and karyolysis, was observed merely in the tumor after treatment with both ICG@DPDCs injection in combination with NIR laser irradiation, but not in the other three control groups. It confirmed again the significant therapeutic effectiveness of ICG@DPDCs under NIR laser irradiation. Therefore, ICG@DPDCs could be used as a powerful photothermal agent for in vivo PTT treatment of cancer.

3.10. Toxicology. To evaluate the in vivo toxicity of the ICG@DPDCs to healthy tissue, healthy mice were intravenously injected with the NPs at a dose of 20 mg/kg, which is equal to that of the imaging/therapy dose. Serum biochemistry assays in Figure 9A showed that hematological parameters including white blood cells (WBC), red blood cells (RBC), platelets (PLT), and neutrophile granulocyte (GRN) have slight fluctuation in the early stage after injection. Nevertheless, all measured hematological parameters in ICG@DPDCs injected mice recovered to the normal ranges after 10 days post injection. Change of mice body weight was also investigated, as shown in Figure 9B. Throughout the period of the study, neither mouse death nor loss of body weight was observed for those mice administrated with ICG@DPDCs. In addition, histological section of liver, heart, spleen, kidney, and lung with H&E staining showed normality in the cellular structures as untreated control group, and neither noticeable organ damage nor inflammation could be observed (Figure 9C). All results ensure that ICG@DPDCs can be a safe agent for medical application.

4. CONCLUSION

A promising theranostic nanoparticle of ICG@DPDCs-^{177}Lu was successfully fabricated for NIR fluorescence/nuclear dual-modality imaging and photothermal ablation of cancer. The cerasome encapsulated ICG showed excellent improvement in photostability and blood circulation time as compared to free ICG molecules and can induce intense temperature elevation under NIR laser exposure. Both in vivo nuclear and fluorescence imaging demonstrated the high tumor targeting efficiency of ICG@DPDCs-^{177}Lu. Experiments in vitro and in vivo confirmed that ICG@DPDCs could effectively ablate cancer cells through photothermal effects. Besides, the strategy of labeling cerasomes with theranostic radionuclide ^{177}Lu enabled the ability of the ^{177}Lu-labeled cerasomes to be used for radionuclide cancer therapy and even the combined therapy. The ability to track the uptake of cerasomes on a whole body basis could provide researchers with an excellent tool for developing cerasome-based therapeutic agents.

ASSOCIATED CONTENT

Supporting Information

The Supporting Information is available free of charge on the ACS Publications website at DOI: 10.1021/acsami.5b07856.

Figures showing mass spectra, FTIR spectra, labeling efficiency, stability, hydrodynamic diameter, and fluorescence intensity; tables of biodistribution and tissue ratios (PDF)

AUTHOR INFORMATION

Corresponding Authors

*E-mail: zhifei.dai@pku.edu.cn.
*E-mail: wangfan@bjmu.edu.cn.
*E-mail: jie.tian@ia.ac.cn.

Author Contributions

#L.J. and J.S. contributed equally to this work.

Notes

The authors declare no competing financial interest.

ACKNOWLEDGMENTS

This work was financially supported by the State Key Program of the National Natural Science of China (no. 81230036), the National High Technology Research and Development Program of China (no. 2013AA032201), the National Natural Science Foundation of China (nos. 21273014, 81321003, and 81420108019), the National Natural Science Foundation for Distinguished Young Scholars (nos. 81125011 and 81225011), and the Foundation for Innovative Research Groups.

REFERENCES

(1) Weissleder, R.; Mahmood, U. Molecular Imaging. *Radiology* **2001**, *219*, 316−333.
(2) Weissleder, R. Molecular Imaging in Cancer. *Science* **2006**, *312*, 1168−1171.
(3) Rudin, M.; Weissleder, R. Molecular Imaging in Drug Discovery and Development. *Nat. Rev. Drug Discovery* **2003**, *2*, 123−131.
(4) Jarzyna, P. A.; Gianella, A.; Skajaa, T.; Knudsen, G.; Deddens, L. H.; Cormode, D. P.; Fayad, Z. A.; Mulder, W. J. M. Multifunctional Imaging Nanoprobes. *Wiley Interdiscip. Rev.: Nanomed. Nanobiotechnol.* **2010**, *2*, 138−150.
(5) Ke, H.; Wang, J.; Dai, Z.; Jin, Y.; Qu, E.; Xing, Z. Gold-Nanoshelled Microcapsules: a Theranostic Agent for Ultrasound Contrast Imaging and Photothermal Therapy. *Angew. Chem., Int. Ed.* **2011**, *50*, 3017−3021.
(6) Sun, Y.; Cao, W.; Li, S.; Jin, S.; Hu, K.; Hu, L.; Ultrabright. and Multicolorful Fluorescence of Amphiphilic Polyethyleneimine Polymer Dots for Efficiently Combined Imaging and Therapy. *Sci. Rep.* **2013**, *3*, 3036.
(7) Sanvicens, N.; Marco, M. P. Multifunctional Nanoparticles–Properties and Prospects for Their Use in Human Medicine. *Trends Biotechnol.* **2008**, *26*, 425−433.
(8) Liong, M.; Lu, J.; Kovochich, M.; Xia, T.; Ruehm, S. G.; Nel, A. E.; Tamanoi, F.; Zink, J. I. Multifunctional Inorganic Nanoparticles for Imaging, Targeting, and Drug Delivery. *ACS Nano* **2008**, *2*, 889−896.
(9) Louie, A. Multimodality Imaging Probes: Design and Challenges. *Chem. Rev.* **2010**, *110*, 3146−3195.
(10) Kong, G.; Anyarambhatla, G.; Petros, W. P.; Braun, R. D.; Colvin, O. M.; Needham, D.; Dewhirst, M. W. Efficacy of Liposomes and Hyperthermia in a Human Tumor Xenograft Model: Importance of Triggered Drug Release. *Cancer Res.* **2000**, *60*, 6950−6957.
(11) Tian, B.; Al-Jamal, W. T.; Al-Jamal, K. T.; Kostarelos, K. Doxorubicin-Loaded Lipid-Quantum Dot Hybrids: Surface Topography and Release Properties. *Int. J. Pharm.* **2011**, *416*, 443−447.

DOI: 10.1021/acsami.5b07856
ACS Appl. Mater. Interfaces 2015, 7, 22095−22105

(12) Liang, X. L.; Gao, J.; Jiang, L. D.; Luo, J. W.; Jing, L. J.; Li, X. D.; Jin, Y. S.; Dai, Z. F. Nanohybrid Liposomal Cerasomes with Good Physiological Stability and Rapid Temperature Responsiveness for HIFU Triggered Local Chemotherapy of Cancer. *ACS Nano* **2015**, *9*, 1280−1293.
(13) Li, Y. Y.; Zheng, S. Q.; Liang, X. L.; Jin, Y. S.; Wu, Y. D.; Bai, H. C.; Liu, R. F.; Dai, Z. F.; Liang, Z. C.; Shi, T. J. Doping Hydroxylated Cationic Lipid into PEGylated Cerasome boosts *In vivo* siRNA Transfection Efficacy. *Bioconjugate Chem.* **2014**, *25*, 2055−2066.
(14) Liang, X. L.; Li, X. D.; Jing, L. J.; Xue, P.; Jiang, L. D.; Ren, Q. S.; Dai, Z. F. Design and Synthesis of Lipidic Organoalkoxysilane for Self-assembly of Liposomal Nanohybrid Cerasomes with Controlled Drug Release Properties. *Chem. - Eur. J.* **2013**, *19*, 16113−16121.
(15) Phillips, D. Light Relief: Photochemistry and Medicine. *Photochem. Photobiol. Sci.* **2010**, *9*, 1589−1596.
(16) Chen, J.; Saeki, F.; Wiley, B. J.; Chang, H.; Cobb, M. J.; Li, Z. Y.; Au, L.; Zhang, H.; Kimmey, M. B.; Li, X.; Xia, Y. Gold Nanocages: Bioconjugation and Their Potential Use as Optical Imaging Contrast Agents. *Nano Lett.* **2005**, *5*, 473−477.
(17) Chen, J.; Wang, D.; Xi, J.; Au, L.; Siekkinen, A.; Warsen, A.; Li, Z.-Y.; Zhang, H.; Xia, Y.; Li, X. Immuno Gold Nanocages with Tailored Optical Properties for Targeted Photothermal Destruction of Cancer Cells. *Nano Lett.* **2007**, *7*, 1318−1322.
(18) Sherlock, S. P.; Tabakman, S. M.; Xie, L. M.; Dai, H. J. Photothermally Enhanced Drug Delivery by Ultrasmall Multifunctional FeCo/Graphitic Shell Nanocrystals. *ACS Nano* **2011**, *5*, 1505−1512.
(19) Yuan, H.; Fales, A. M.; Vo-Dinh, T. TAR Peptide-Functionalized Gold Nanostars: Enhanced Intracellular Delivery and Efficient NIR Photothermal Therapy Using Ultralow Irradiance. *J. Am. Chem. Soc.* **2012**, *134*, 11358−11361.
(20) Hirsh, L. R.; Stafford, R. J.; Bankson, J. A.; Sersher, S. R.; Rivera, B. R.; Price, E.; Hazle, J. D.; Halas, N. J.; West, J. L. Nanoshell-Mediated near-Infrared Thermal Therapy of Tumors under Magnetic Resonance Guidance. *Proc. Natl. Acad. Sci. U. S. A.* **2003**, *100*, 13549−13554.
(21) Huang, X.; El-Sayed, I. H.; Qian, W. M.; El-Sayed, A. Cancer Cell Imaging and Photothermal Therapy in the Near-Infrared Region by Using Gold Nanorods. *J. Am. Chem. Soc.* **2006**, *128*, 2115−2120.
(22) Lee, J.; Yang, J.; Ko, H.; Oh, S. J.; Kang, J.; Son, J. H.; Lee, K.; Lee, S. W.; Yoon, H. G.; Suh, J. S.; Huh, Y. M.; Haam, S. Multifunctional Magnetic Gold Nanocomposites: Human Epitherial Cancer Detection via Magnetic Resonance Imaging and Localized Synchronous Therapy. *Adv. Funct. Mater.* **2008**, *18*, 258−264.
(23) Fass, L. Imaging and Cancer: A Review. *Mol. Oncol.* **2008**, *2*, 115−152.
(24) Jaffray, D. A. Image-Guided Radiotherapy: From Current Concept to Future Perspectives. *Nat. Rev. Clin. Oncol.* **2012**, *9*, 688−699.
(25) Liang, X. L.; Li, Y. Y.; Li, X. D.; Jing, L. J.; Deng, Z. J.; Yue, X. L.; Li, C. H.; Dai, Z. F. PEGylated Polypyrrole Nanoparticles Conjugating Gadolinium Chelates for Dual-Modal MRI/Photoacoustic Imaging Guided Photothermal Therapy of Cancer. *Adv. Funct. Mater.* **2015**, *25*, 1451−1462.
(26) Jin, Y. S.; Wang, J. R.; Ke, H. T.; Wang, S. M.; Dai, Z. F. Graphene Oxide Modified PLA Microcapsules Containing Gold Nanoparticles for Ultrasonic/CT Bimodal Imaging Guided Photothermal Tumor Therapy. *Biomaterials* **2013**, *34*, 4794−4802.
(27) Guo, C. X.; Jin, Y. S.; Dai, Z. F. Multifunctional Ultrasound Contrast Agents for Imaging Guided Photothermal Therapy. *Bioconjugate Chem.* **2014**, *25*, 840−854.
(28) Jing, L. J.; Liang, X. L.; Li, X. D.; Lin, L.; Yang, Y. B.; Yue, X. L.; Dai, Z. F. Mn-porphyrin Conjugated Au Nanoshells Encapsulating Doxorubicin for Potential Magnetic Resonance Imaging and Light Triggered Synergistic Therapy of Cancer. *Theranostics* **2014**, *4*, 858−871.
(29) Ke, H. T.; Wang, J. R.; Tong, S.; Jin, Y. S.; Wang, S. M.; Qu, E. Z.; Bao, G.; Dai, Z. F. Gold Nanoshelled Liquid Perfluorocarbon Magnetic Nanocapsules: a Nanotheranostic Platform for Bimodal Ultrasound/Magnetic Resonance Imaging Guided Photothermal Tumor Ablation. *Theranostics* **2014**, *4*, 12−23.
(30) Chen, Y.; Chen, H. R.; Shi, J. L. In Vivo Bio-Safety Evaluations and Diagnostic/Therapeutic Applications of Chemically Designed Mesoporous Silica Nanoparticles. *Adv. Mater.* **2013**, *25*, 3144−3176.
(31) Funovics, M.; Weissleder, R.; Tung, C. H. Protease Sensors for Bioimaging. *Anal. Bioanal. Chem.* **2003**, *377*, 956−963.
(32) Sakka, S. G. Assessing liver function. *Curr. Opin. Crit. Care* **2007**, *13*, 207−214.
(33) Chen, W. R.; Liu, H.; Ritchey, J. W.; Bartels, K. E.; Lucroy, M. D.; Nordquist, R. E. Effect of Different Components of Laser Immunotherapy in Treatment of Metastatic Tumors in Rats. *Cancer Res.* **2002**, *62*, 4295−4299.
(34) Sheng, Z. H.; Hu, D. H.; Zheng, M. B.; Zhao, P. F.; Liu, H. L.; Gao, D. Y.; Gong, P.; Gao, G. H.; Zhang, P. F.; Ma, Y. F.; Cai, L. T. Smart Human Serum Albumin-Indocyanine Green Nanoparticles Generated by Programmed Assembly for Dual-Modal Imaging-Guided Cancer Synergistic Phototherapy. *ACS Nano* **2014**, *8*, 12310−12322.
(35) Dzurinko, V. L.; Gurwood, A. S.; Price, J. R. Intravenous and Indocyanine Green Angiography. *Optometry* **2004**, *75*, 743−755.
(36) Yoneya, S.; Saito, T.; Komatsu, Y.; Koyama, I.; Takahashi, K.; Duvoll-Young, J. Binding Properties of Indocyanine Green in Human Blood. *Invest. Ophthalmol. Visual Sci.* **1998**, *39*, 1286−1290.
(37) Saxena, V.; Sadoqi, M.; Shao, J. Degradation Kinetics of Indocyanine Green in Aqueous Solution. *J. Pharm. Sci.* **2003**, *92*, 2090−2097.
(38) Mordon, S.; Devoisselle, J. M.; Soulie-Begu, S.; Desmettre, T. Indocyanine Green: Physicochemical Factors Affecting its Fluorescence in vivo. *Microvasc. Res.* **1998**, *55*, 146−152.
(39) Desmettre, T.; Devoisselle, J. M.; Mordon, S. Fluorescence Properties and Metabolic Features of Indocyanine Green (ICG) as Related to Angiography. *Surv. Ophthalmol.* **2000**, *45*, 15−27.
(40) Zheng, C. F.; Zheng, M. B.; Gong, P.; Jia, D. X.; Zhang, P. F.; Shi, B. H.; Sheng, Z. H.; Ma, Y. F.; Cai, L. T. Indocyanine Green-Loaded Biodegradable Tumor Targeting Nanoprobes for in Vitro and in Vivo Imaging. *Biomaterials* **2012**, *33*, 5603−5609.
(41) Manchanda, R.; Fernandez-Fernandez, A.; Nagesetti, A.; McGoron, A. J. Preparation and Characterization of a Polymeric (PLGA) Nanoparticulate Drug Delivery System with Simultaneous Incorporation of Chemotherapeutic and Thermo-optical Agents. *Colloids Surf., B* **2010**, *75*, 260−267.
(42) Yaseen, M. A.; Yu, J.; Wong, M. S.; Anvari, B. Laser-induced heating of dextran-coated mesocapsules containing indocyanine green. *Biotechnol. Prog.* **2007**, *23*, 1431−1440.
(43) Ma, Y.; Tong, S.; Bao, G.; Gao, C.; Dai, Z. F. Indocyanine Green Loaded SPIO Nanoparticles with Phospholipid-PEG Coating for Dual-modal Imaging and Photothermal Therapy. *Biomaterials* **2013**, *34*, 7706−7714.
(44) Ma, Y.; Liang, X. L.; Tong, S.; Bao, G.; Ren, Q. S.; Dai, Z. F. Gold Nanoshell Nanomicelles for Potential Magnetic Resonance Imaging, Light-Triggered Drug Release, and Photothermal Therapy. *Adv. Funct. Mater.* **2013**, *23*, 815−822.
(45) Zheng, X.; Xing, D.; Zhou, F.; Wu, B.; Chen, W. R. Indocyanine Green-Containing Nanostructure as Near Infrared Dual-Functional Targeting Probes for Optical Imaging and Photothermal Therapy. *Mol. Pharmaceutics* **2011**, *8*, 447−456.
(46) He, Q. J.; Zhang, Z. W.; Gao, F.; Li, Y. P.; Shi, J. L. In Vivo Biodistribution and Urinary Excretion of Mesoporous Silica Nanoparticles: Effects of Particle Size and PEGylation. *Small* **2011**, *7*, 271−280.

DOI: 10.1021/acsami.5b07856
ACS Appl. Mater. Interfaces 2015, 7, 22095−22105